J Mater Sci (2022) 57:170–184

Ceramics

Red-emitting $BaAl_2O_4:Eu^{3+}$ synthesized via Pechini and sol–gel routes: a comparison of luminescence and structure

Nagyla A. Oliveira[1,2,3], Airton G. Bispo-Jr[3], Sergio A. Marques Lima[1,*], and Ana M. Pires[1,2,*]

[1] School of Technology and Sciences, São Paulo State University (Unesp), R. Roberto Simonsen, 305, Presidente Prudente, SP 19060-900, Brazil

[2] Institute of Biosciences, Humanities and Exact Sciences, São Paulo State University (Unesp), São José Do Rio Preto, SP 15054-000, Brazil

[3] Institute of Chemistry, University of Campinas, UNICAMP, Campinas, Sao Paulo 13083-970, Brazil

Received: 7 July 2021
Accepted: 13 October 2021
Published online: 3 January 2022

ABSTRACT

UV-to-red downshifting phosphors such as $BaAl_2O_4:Eu^{3+}$ find broad range of application in sensors, displays, and in solid-state lighting, yet new synthetic routes to improve their luminescence are envisaged. In this regard, herein, it is introduced two new methods to synthesize this environmentally friendly $BaAl_2O_4:Eu^{3+}$, by an adapted sol–gel route and a modified Pechini synthesis. Additionally, a systematic study was carried out about the Eu^{3+} doping concentration and charge compensation effects on the structural, morphological and spectroscopic features. Both routes enabled high-crystalline and nanostructured phosphors displaying optic bandgap near to 4.4 eV, although the sol–gel route also led to low amounts of $BaCO_3$ spurious phase. Upon UV (250 nm) excitation, all Eu^{3+}-doped samples emit red light displaying high emission color purity, characteristic of the $^5D_0 \rightarrow {}^7F_{0\text{-}4}$ electronic transitions of Eu^{3+}. The Pechini method led to the highest intrinsic emission quantum yield (85% for the 3%-doped sample). Eu^{3+} replaces Ba^{2+} within the $BaAl_2O_4$ lattice, but in the sol–gel-derived samples, the dopant may also replace Ba^{2+} into the $BaCO_3$ spurious phase, confirming that the Pechini route is the best one to optimize the luminescence and structure of the phosphor.

Handling Editor: Andrea de Camargo.

Address correspondence to E-mail: sergio.lima@unesp.br; ana.maria@unesp.br

https://doi.org/10.1007/s10853-021-06633-3

GRAPHICAL ABSTRACT

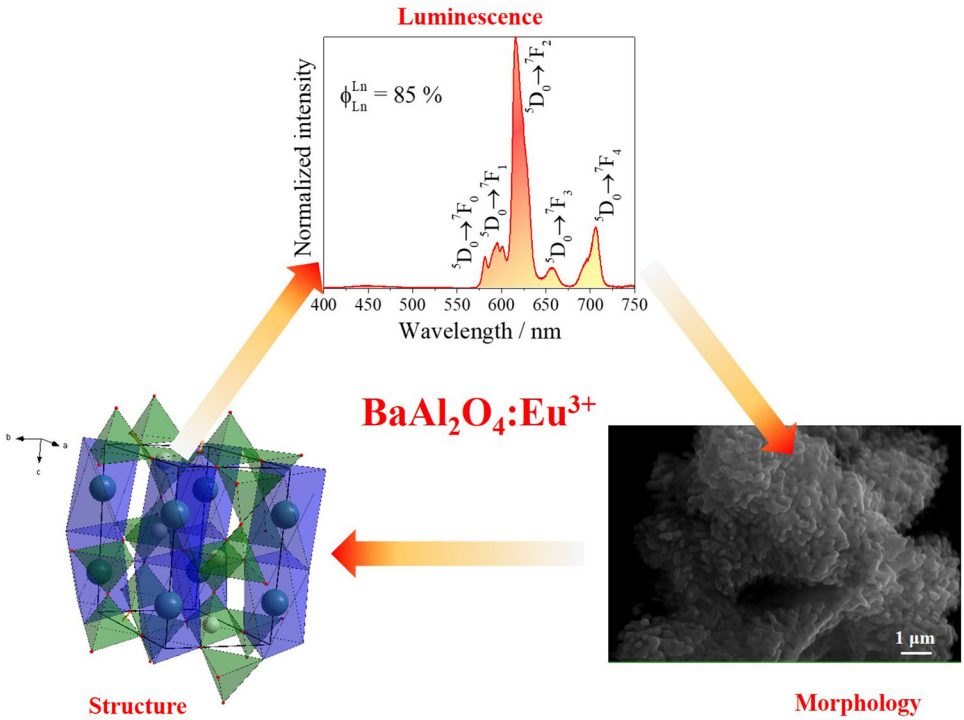

Introduction

UV-to-red downshifting emitting phosphors find a broad range of applications [1] in televisions [2, 3], solid-state lighting [4, 5], multifunctional light-emitting diodes [6, 7], field emission displays [2, 3], photonics, plasma display panels (PDPs) [2, 3], fiber amplifiers [8], optoelectronics for image storage [9], and detectors of energy radiation [9]. Although the main commercially available red-emitting phosphors, i.e., $Zn_{1-x}Cd_xS:Ag^+$ or $Y_2O_2S:Eu^{3+}$, feature high overall emission quantum yield, some drawbacks must still be overcome, especially that related to their composition based on heavy metals and sulfur atom that is released over time of usage [3, 10]. In this regard, new strategies toward the synthesis of environmentally friendly red-emitting phosphors displaying intense luminescence are of large societal relevance.

Among several red-emitting systems, $BaAl_2O_4:Eu^{3+}$ stands out due to its environmentally friendly properties, chemical, thermal, and photostability, relatively low cost of production, simplicity of the synthesis methods, and similarity between the ionic radius of Ba^{2+} and Eu^{3+}, altogether making $BaAl_2O_4$ a desirable host. [11] Moreover, Eu^{3+} is a well-known luminescent activator characterized by narrow emission bands within the red spectral region that arise from intraconfigurational $4f \rightarrow 4f$ electronic transitions [12]. Due to these features, several studies have shown the potential application of $BaAl_2O_4:Eu^{3+}$ in solid-state lighting, scintillation, or dosimetry [13, 14]. Yet, some issues need to be addressed concerning the development of new synthetic strategies toward the enhancement of the Eu^{3+} luminescence and the charge imbalance between Eu^{3+} and Ba^{2+}, which leads to structural defects that often quench the radiative process arising from the $^5D_0$ emitting state of Eu^{3+}. [15]

Some routes for the obtention of $BaAl_2O_4:Eu^{3+}$ are reported so far, such as methods based on combustion [13, 16], conventional Pechini [11, 15],

hydrothermal [17], floating zone [13], and protein [18–21] or polyvinyl alcohol [22]-assisted sol–gel. Moreover, methods applied for the synthesis of other Eu^{3+}-doped aluminates are also reported, such as the combustion method used in the $ZnAl_2O_4:Eu^{3+}:Tb^{3+}$ synthesis [23] or the urea-assisted combustion approach for obtaining $CaAl_2O_4:Eu^{3+},Er^{3+}$ [24]. Although some of these routes enable a quite good particle shape and size control, there is not a consensus on which synthesis is the best regarding the enhancement of the Eu^{3+} luminescence. In this regard, we introduce two new routes for the phosphor obtention based on a sol–gel route adapted from the $Ba_2SiO_4:Eu^{3+}$ synthesis [25] and a modified Pechini method using sorbitol instead of the classic ethylene glycol as polymerizing agent, which enhances the Eu^{3+} luminescence according to our previous study for the $Y_2O_3:Eu^{3+},Er^{3+},Yb^{3+}$ phosphor [26]. The justifications behind these selections lie in the relatively low cost, simplicity, achievement of high level of purity, well-crystallized phosphor, and decrease in the annealing temperature compared to solid-state synthesis [27, 28].

Therefore, in this study, $BaAl_2O_4:Eu^{3+}$ red-emitting phosphors were synthesized by two adapted routes, the sol–gel and the Pechini method, by applying a charge compensation mechanism in the Eu^{3+} doping within the $BaAl_2O_4$ lattice. Furthermore, structural, morphological, and spectroscopic studies were performed to evaluate Eu^{3+} site occupancy, influence of concentration on structure and luminescence as well as the mechanism behind energy transfer among Eu^{3+} ions, which is responsible for luminescence quenching by concentration.

Materials and methods

Acetic acid (CH_3COOH, Cinética, 99.7%), citric acid ($C_6H_8O_7$, Fluka analytical, 99.5%), nitric acid (HNO_3, FMaia, 65%), barium acetate ($Ba(CH_3COO)_2$, Vetek, 99%) aluminum nitrate ($Al(NO_3)_3.9H_2O$, Across, 98%), D-sorbitol ($C_6H_{14}O_6$, Aldrich, 99%), aluminum isopropoxide ($C_9H_{21}O_3Al$, Across, 99%), and europium oxide (Eu_2O_3, Aldrich, 99.99%) were used as starting reactants without any further purification.

Modified Pechini synthesis. Stoichiometric amount of $Ba(CH_3COO)_2$ aiming to prepare 0.5000 g of the final product was dissolved in acetic acid (6 mL) under agitation and heating (50 °C), followed by the addition of H_2O (25 mL). After 10 min, stoichiometric amounts of $Al(NO_3)_3$, $Eu(NO_3)_3$ (prepared from the dissolution of Eu_2O_3 in concentrated nitric acid, in the case of the doped samples, and titrated by using EDTA as complexing agent and xylenol orange as indicator), and citric acid (3 mols of citric acid:1 mol of metal) were added, enabling the metal-citrate complex formation. The temperature of the system was kept at ~ 85 °C/1 h until halving the initial volume, and then, sorbitol was added (1 mol of sorbitol:2 mols of metal). The system was kept under stirring and heating until the formation of a clear foamy polymer resin, which was pre-calcined (300 °C) for 2 h in static air. A spongy-like agglomerate, also called "puff," was then obtained [26]. The "puff" precursor was de-agglomerated and sieved at 325 mesh sieves, and annealed at 1000 °C (heating ramp of 5 °C/min) for 2 h in a circulating air atmosphere.

Sol–gel synthesis. Stoichiometric amount of $Ba(CH_3COO)_2$ aiming to prepare 0.5000 g of the final product was dissolved in acetic acid (1.5 mL) under agitation and heating (50 °C), followed by the addition of H_2O (10 mL). After 10 min, stoichiometric quantities of $Eu(CH_3COO)_3$ solution (previously prepared from the dissolution of Eu_2O_3 in CH_3COOH) was added. In the sequence, $C_9H_{21}O_3Al$ in stoichiometric proportions was added under vigorous stirring and heating (80 °C) until complete dissolution and gel formation. This gel was dried in an oven for 1 h to yield the xerogel precursor that was thermally treated at 300 °C in a static air atmosphere (heating ramp of 5 °C/min for 2 h) [25]. Finally, the precursor was de-agglomerated in a mortar and annealed at 1,000 °C in a circulating air atmosphere (heating ramp of 5 °C/min) for 2 h.

Table 1 Doping proportions. The Eu^{3+} concentration was isoelectronically varied from 1 to 7%,

xDp%[a]	n_{Ba}	n_{Eu}	xCh% [b]	xAt% [c]
1	0.985	0.01	1.5	1.0
3	0.955	0.03	4.5	3.0
5	0.925	0.05	7.5	5.1
7	0.895	0.07	10.5	7.2

a Eu^{3+}-doping percentage in relation to 1 mol of Ba^{2+} in the undoped $BaAl_2O_4$.

b Eu^{3+}-doping percentage in relation to the total cation charge in each sample.

c Eu^{3+}-doping percentage in relation to the total cation mol amount for each sample.

The Eu^{3+} doping concentrations were isoelectronically varied from 1 to 7% (Table 1), i.e., keeping the same overall charge in the $BaAl_2O_4$ matrix, according to the Ba^{2+}, Eu^{3+} and $Al_2O_4^{2-}$ charges ($3n_{Eu^{3+}} + 2n_{Ba^{2+}} = +2$, where $n_{Ba^{2+}}$ and $n_{Eu^{3+}}$ are the mol number of Ba^{2+} and Eu^{3+}, respectively, in the $Ba_{nBa}Eu_{nEu}Al_2O_4$ formula). Samples will be hereafter labeled as PCX or SGX, where SG = sol–gel-derived samples, PC = Pechini-derived samples, and X = Eu^{3+}-doping percentage.

Characterization. All samples were characterized, from the structural point of view by X-ray diffraction (XRD) using a SHIMADZU diffractometer model XDR-6000, Cu(K_α) radiation (λ = 1.5406 Å), interval of 10°—80° (2θ), increment of 0.02° and integration time of 0.6 s. The crystallite size of samples was evaluated via Scherrer method, according to Eq. 1 [29], where βp is the width at half maximum in radians of a given (h k l) reflection peak due to the grain size (ε) in the corresponding (h k l) direction, and c is a constant that depends on the reflection symmetry which usually is given as 1. To calculate the crystallite size, the three most intense peaks related to (2 0 0), (2 0 2), and (2 2 0) plans at 19.7°, 28.2° and 34.2° were considered, respectively:

$$\beta_p = \frac{c\lambda}{\varepsilon \cos\theta} \tag{1}$$

Thermogravimetry of precursors doped with 1% was measured by using an SDT-Q600TA instrument with a heating rate of 10 °C/min from 25 °C to 1,400 °C in air flow (100 mL/min). SEM measurements were carried out using a scanning electron microscope CARLS ZEISS, model EVO LS15 with a secondary electron detector (SE), 25.00 KX of magnification, EHT of 30.00 kV. For that, an ethanolic suspension containing particles was deposited on a glass cover plate, which was fixed with double carbon facing tape on a stub and then metalized with gold using a Quorum sputtering, model Q 150R ES.

UV–Vis diffuse reflectance was measured in a PERKIN ELMER LAMBDA 1050 spectrophotometer. From the diffuse reflectance spectrum, the optical bandgap was estimated through a graphic of $(\alpha h\nu)^n$ versus the energy of the incident photon (eV), Figure S1 (Supplementary Material), where n is equal to 2 for direct electronic transitions or 0.5 for indirect transitions between the valence and conduction bands [30]. α is the ratio of the scattering (K) and absorption (S) coefficients determined from the Kubelka–Munk method [31], Eq. 2, where R is the reflectance observed for different incident energies.

$$\alpha = \frac{K}{S} = \frac{(1-R)^2}{4R} \tag{2}$$

Photoluminescence measurements at 300 K or at 77 K were carried out in a Horiba Jobin Yvon spectrometer Fluorolog-3 with a Xe lamp (450 W) source with double excitation monochromator. The slits were placed at 1.1 and 0.7 mm for excitation and emission, respectively. The emission decay curves were carried out in a phosphorimeter equipped with Xe (5 J/pulse) lamp. By applying the Judd–Ofelt theory that describes the behavior of *f-f* electronic transitions in Ln^{3+} by a forced electric dipole mechanism, it is possible to infer on the radiative decay probabilities (A_{rad}) of the $^5D_0$ emitting state and the Ω_2 and the Ω_4 intensity parameters. A_{rad} was calculated by using Eq. 3, where $A_{01} = 14.65\, n^3$ in s^{-1} [32], and n is the refractive index, equal to 1.657 for $BaAl_2O_4$ [33], I is the integrated area under the $^5D_0 \rightarrow {}^7F_J$ transitions in the emission spectra, and $h\upsilon_{0\text{-}J}$ is the energy barycenter of the electronic transition. Thus, A_{rad} is the sum of radiative rates of all electronic transitions coming from the $^5D_0$ state ($A_{rad} = \sum A_{0-J}$).

$$A_{0-\lambda} = A_{0-J} = A_{01}\frac{I_{0-J}}{I_{0-1}}\frac{h\upsilon_{0-1}}{h\upsilon_{0-J}} \tag{3}$$

The intensity parameters were calculated by using Eq. 4, where $\left|{}^7F_J U^{(\lambda)} {}^5D_0\right|^2$ represents the square reduced matrix elements whose values are equal to 0.0032 to Ω_2 and 0.0023 to Ω_4; h is the Planck's constant, e is the electron charge, c is the speed of light in vacuum, ω *is the* angular frequency of the incident radiation field, ε_0 is vacuum permittivity constants, and X is the Lorentz local field correction equal to $n(n^2+2)^2/9$ [34].

$$\Omega_\lambda = \frac{3hc^3 A_{0\lambda}}{8\pi e^2 \omega^3 \chi \left|\left\langle {}^7F_J \| U^{(\lambda)} \| {}^5D_0 \right\rangle\right|^2} \tag{4}$$

Results and discussion

Structural characterization

Precursors of both methods were characterized by thermogravimetry aiming the determination of the $BaAl_2O_4$ phase formation temperature, Fig. 1. For the

sol–gel-derived precursor, the thermal event starting at 200 °C and peaking at 280 °C is correlated with the thermal decomposition of the organic matter coming from the precursors. On the other hand, for the Pechini precursor, the first thermal event with maximum at 100 °C is due to water evaporation, while the second one at 200 °C is related to the thermal degradation of nitrates and organic matter. Due to its high basicity, Ba^{2+} tends to form $BaCO_3$ in such environmental conditions, whose formation ranges within 400–500 °C [35]. For both precursors, the thermal event at 900 °C is associated with the $BaAl_2O_4$ phase formation, which was confirmed by XRD data.

The X-ray diffraction patterns of samples synthesized at 1,000 °C, Fig. 2, are indexed as the hexagonal $BaAl_2O_4$ structure (JCPDS-17–0306), space group $P6_322$. All diffraction peaks are sharp and well defined, confirming that the phase is highly crystalline. However, for the sol–gel-derived samples with low Eu^{3+} doping percentage, a low-intensity peak at 24° is observed, characteristic of the diffraction plan of the $BaCO_3$ (JCPDS-45–1471) spurious phase (see the magnification of this region in supplementary material, Figure S2). The $BaCO_3$ phase formation is common for compounds with high basicity cations such as Ba^{2+}, being intermediated by CO_2 coming from organic matter decomposition and/or air atmosphere, as reported for the synthesis of $BaTiO_3$ [36, 37] or Ba_2SiO_4 [25]. The sol–gel route itself normally leads to particles displaying porous surface that can easily react with CO_2 from atmosphere, favoring the formation of carbonate groups. Moreover, the sol–gel-derived xerogel precursor based on Si–O bonds is often reported [38–40] as a porous structure that can confine organic groups, making it difficult for CO_2 to be released due to thermolysis, which favors the $BaCO_3$ formation. Interestingly, it is observed a smooth peak at 24° in the XRD data reported by Chatterjee and co-workers for sol–gel-derived $BaAl_2O_4$ [15], which may be assigned to the $BaCO_3$ phase.

In $BaAl_2O_4$, Ba^{2+} occupies two different sites with the same coordination number (CN = 9), Fig. 2c, but in the Ba1 site (C_3 point group), the Ba–O bond distance lies within the 2.86 – 2.87 Å, while for the Ba2 site (C_1 point group), the Ba–O bond distance is 2.69 Å. Moreover, the Ba1 site occurs at about three times more than the Ba2 one. On the other hand, Al^{3+} is inserted into four different tetrahedral sites featuring Al-O bond distances close to 1.77, 1.74, 1.72, and 1.83 Å. [9] Since Eu^{3+} (ionic radius of 126 pm, CN = 9) and Ba^{2+} (ionic radius of 161 pm) have a better ionic radii match, Eu^{3+} replaces Ba^{2+} sites in the $BaAl_2O_4$ structure according to the Hume-Rothery rules, which states that the ionic radius difference between solvent and solute ions should be close to 15% [9]. It is worth pointing out that although the ionic radii difference between Eu^{3+} and Ba^{2+} is larger than 15%, doping takes place since no Eu_2O_3 diffraction peaks are observed in the XRD diffractogram (considering the detection limit of 1wt.%), Fig. 2, confirming the formation of a solid solution. Interestingly, Ba^{2+} replacement by lanthanide(III) in inorganic matrices has already been reported, for

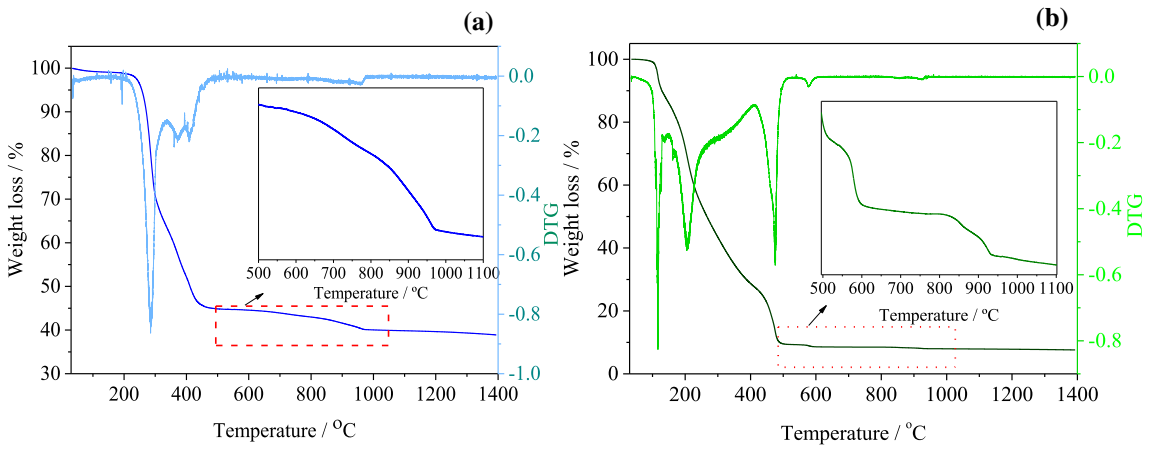

Figure 1 Thermogravimetric curves (TG) and first-order derivate (DTG) of **a** sol–gel and **b** Pechini precursors, both doped with 1% of Eu^{3+}.

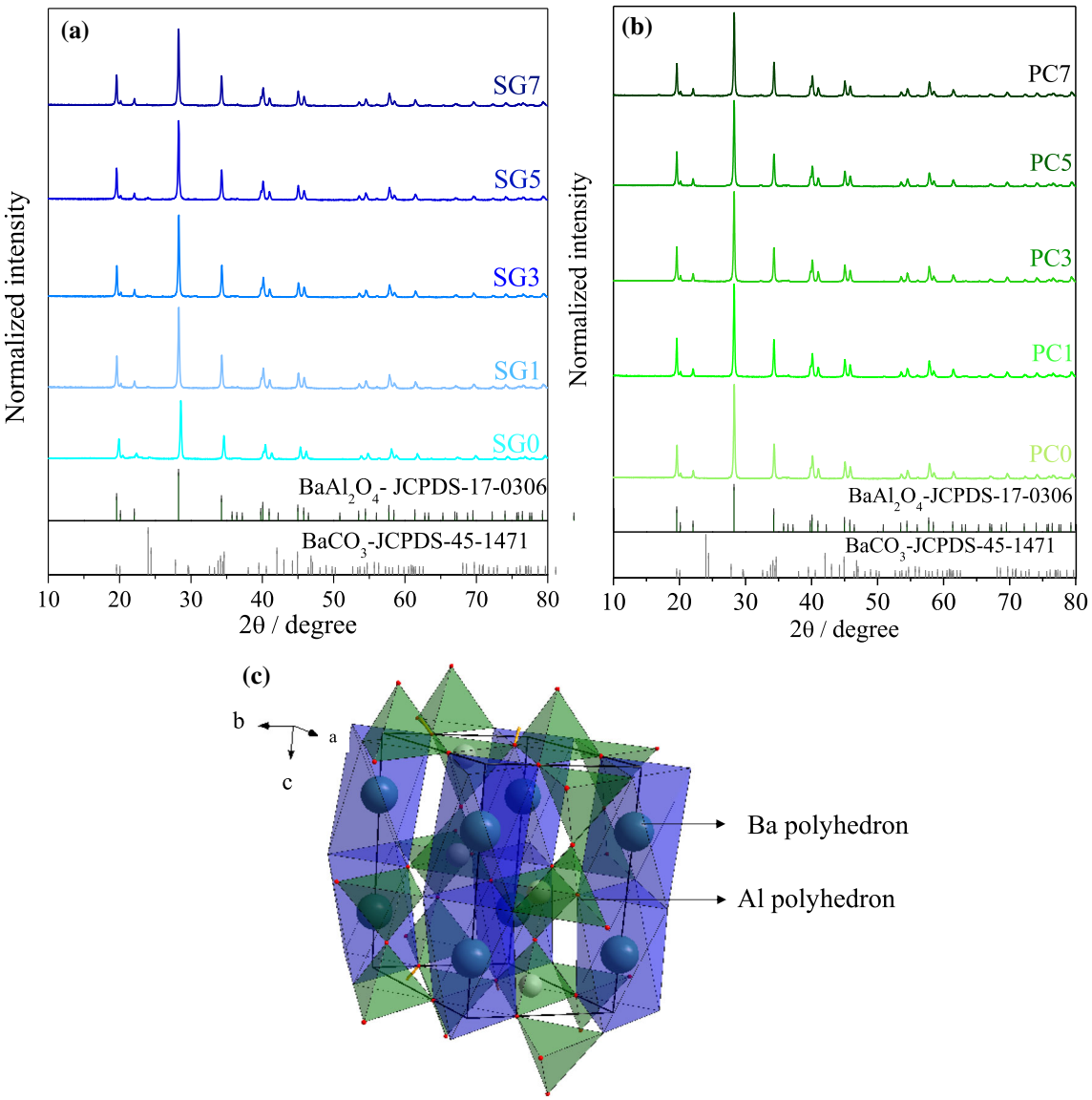

Figure 2 X-ray diffraction pattern of the Eu^{3+}-doped $BaAl_2O_4$ samples obtained from **a** sol–gel and **b** Pechini routes. **c** $BaAl_2O_4$ crystalline structure based on the CIF file available on Inorganic Crystal Structure Database (ICSD).

instance, for the $Ba_2SiO_4:Eu^{3+}$ [25] and $Ba_2SiO_4:Tb^{3+}$ [4] systems.

From the analysis of Fig. 2, there is no shift of the diffraction peaks related to the $BaAl_2O_4$ phase in the XRD data for the Pechini-derived samples (Figure S2), suggesting that neither the doping nor the synthetic route led to significant changes in the $BaAl_2O_4$ crystalline structure. Yet, for the sol–gel-prepared ones, slight shifts of the diffraction peaks (Figure S2) may be correlated with the spurious phase that influences the $BaAl_2O_4$ lattice organization.

The crystallite size values determined by the Scherrer equation shown in Table 2 are comparable with those ones of other oxide compounds prepared by humid routes [35, 41, 42] and they also reveal a non-isotropic crystallite grown tendency. There is a tendency of increasing the average crystallite size due to the doping for the SG samples, while the values for the Pechini-derived ones have no statistical change. In this case, changes in the crystallite size may be correlated with two factors, the $BaCO_3$ spurious phase (present only in the SG1 and SG3 samples) and the doping amount. The amount of $BaCO_3$ phase may control the boundaries during the synthesis,

Table 2 Crystallite size (± 1 nm) for the three most intense diffraction peaks and average crystallite size for samples

Sample	Crystallite size			
	Plan (2 0 0)	Plan (2 0 2)	Plan (2 2 0)	Average size
PC0	47	44	43	45
PC1	52	47	45	48
PC3	50	46	44	47
PC5	48	44	40	44
PC7	47	44	41	44
SG0	41	43	42	42
SG1	50	45	41	45
SG3	49	46	43	46
SG5	54	47	43	47
SG7	53	47	44	48

determining the mass transfer through the grain boundaries [43]. On the other hand, since Eu^{3+} and Ba^{2+} have quite different ionic radii, the increase in the doping content may lead to smooth local changes around Eu^{3+} local sites, which influence the structure formation and as a consequence the crystallite size.

Representative SEM images of PC1 and PC5 samples, Fig. 3a and b, exhibit particle agglomerates, which are common to quite high-temperature annealing processes, resulting in sintered surfaces [44]. On the other hand, the sol–gel-derived particles, Fig. 3c and d, feature different shapes and sizes, with spheroidal-like particles on the surface. This behavior is associated with the acid-catalyzed sol–gel route, which typically leads to particle agglomerates from the coalescence of spheres [45]. Thus, the sol–gel synthesis enables better shape control, although both methods form a nanostructured bulk.

Optical band gap evaluation

The optical absorption of all samples was evaluated through diffuse reflectance spectroscopy, Fig. 4. For all doped samples, three bands are noticed in the diffuse reflectance spectra; the first one at 220 nm (also noticed in the excitation spectra, Fig. 5) is assigned to the $Eu^{3+} \rightarrow O^{2-}$ charge transfer band (CTB), and its relative intensity enhances as the Eu^{3+} content increases; the second at 262 nm is the electronic transition from the valence band (VB) to the conduction band (CB) of the matrix (the optical bandgap), and the third at 361 nm, also observed in

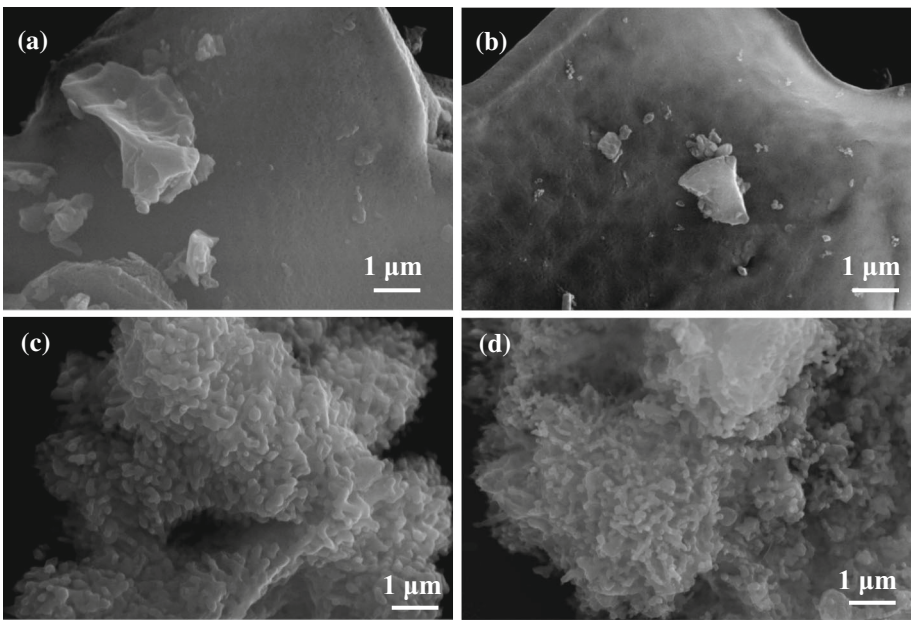

Figure 3 SEM images of **a** PC1, **b** PC5, **c** SG1, and **d** SG3 samples.

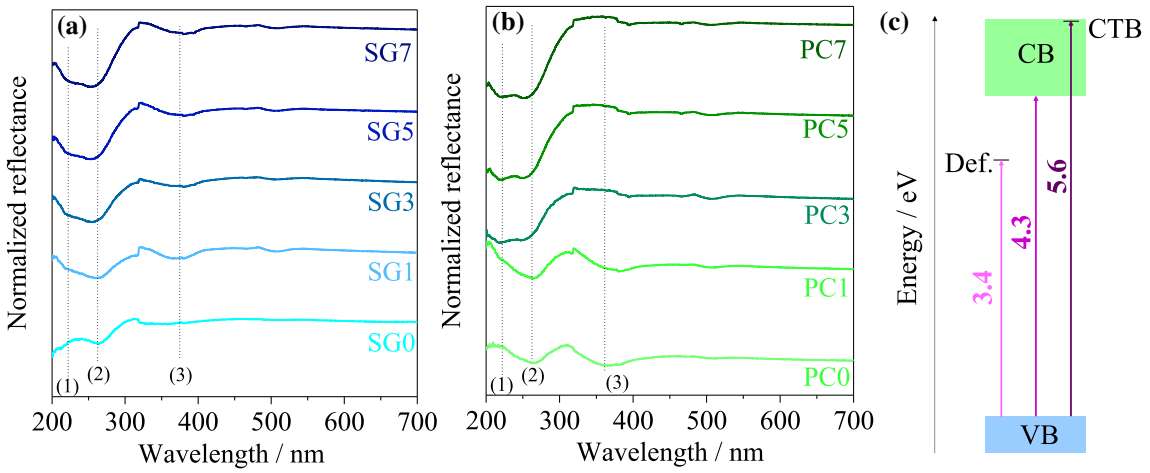

Figure 4 Diffuse reflectance spectra of **a** sol–gel and **b** Pechini-derived samples. **c** Energy diagram representing the absorption transitions. Assignments: (1) $Eu^{3+} \rightarrow O^{2-}$ charge transfer band (CTB). (2) Valence band (VB) → conduction band (CB) transition. (3) Defect-related matrix absorption.

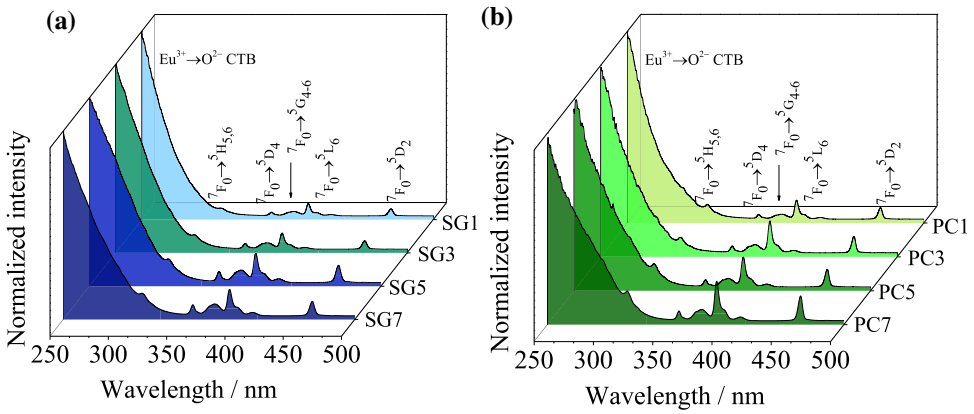

Figure 5 Excitation spectra of the **a** sol–gel and **b** Pechini-derived samples monitored at 616.7 nm.

the non-doped samples, may be associated with absorptions to electronic states arising from structural defects.

Indeed, it is usual to notice absorption in inorganic matrices ranging in the near-UV spectral region due to the presence of traps or intrinsic defects that may arise from the thermal decomposition of organic solvents or organic products of the sol–gel or Pechini syntheses [25, 35]. Moreover, due to the isoelectronic doping, three Ba^{2+} sites are replaced by only two Eu^{3+} ions, leading to one Ba^{2+} vacancy according to Eq. 5. Those vacancies increase the concentration of structural defects, leading to the appearance of defect-related electronic states within the forbidden band, as represented in Fig. 4c. For sol–gel-derived samples, the higher is the doping percentage, the stronger is the defect-related absorption band at 350 nm, ensuring that the structural defect concentration increases. On the other hand, for Pechini-based samples, this behavior is not observed due to the larger amount of organic matter within the precursor coming from sorbitol and citric acid, which also induces structural defects, decreasing the importance of defects arising from the doping process.

$$3Ba^{2+} + 2Eu^{3+} \rightarrow V_{Ba} + 2Eu_{Ba}^{\cdot} \quad (5)$$

The optical bandgap of samples was calculated accordingly to the Kubelka–Munk approximation, Figure S1, and the values are statistically the same (4.3 ± 0.1 eV) independent on the doping concentration or the synthesis, in accordance with other values reported so far for the $BaAl_2O_4$ host [46].

Luminescence

The excitation spectra of samples monitored at emission of Eu^{3+}, Fig. 5, are dominated by a broad and intense excitation band within the short-wavelength region assigned to the Laporte's allowed $Eu^{3+} \rightarrow O^{2-}$ CTB, in accordance with reflectance diffuse spectra, confirming that the $BaAl_2O_4$ host sensitizes the Eu^{3+} luminescence. Moreover, the lower-intensity excitation lines ranging in the long-wavelength region are attributed to the Laporte's forbidden intraconfigurational Eu^{3+} *f-f* transitions [47]. In this sense, the phosphors may be excited from the deep UV to the blue spectral window, crossing the near UV spectral region.

The emission spectra of all phosphors, Fig. 6, are characterized by a set of sharp emission bands within the orange-red spectral region assigned to electronic transitions coming from the $^5D_0$ state of Eu^{3+} to $^7F_{0\text{-}4}$ ones, where the band peaking at 617 nm assigned to the $^5D_0 \rightarrow {}^7F_2$ transition is the most intense one [47]. Interestingly, the Pechini-derived phosphors also feature a broad and weak emission band at 420 nm, which is assigned to the matrix emission accordingly to the emission spectrum of the undoped $BaAl_2O_4$ (see Figure S3); this band arises from the aforementioned defect-related electronic states according to the diffuse reflectance data and its stronger intensity in the Pechini-derived phosphors is related to the higher concentration of organic matter in the Pechini synthesis, which may induce a higher concentration of structural defects in the matrix.

From the colorimetric point of view, the emission color of phosphors was characterized by the 1,931 *Commission Internationale de l'éclairage* (CIE) color coordinates, Fig. 6 and Table S1. The emission color of all sol–gel-derived phosphors lies within the red spectral region with color purity near to 100% although, for the Pechini-derived samples, there is a shift toward the pink due to the combination of the weak matrix blue luminescence and the Eu^{3+} characteristic red emission.

Besides the red luminescence, Eu^{3+} may act as a spectroscopic probe since some of its *f-f* electronic transitions are influenced by the ligand field, enabling the evaluation of the local Eu^{3+} microssimetry by the relative intensity and the number of components of emission bands [48]. In the emission spectra shown in Fig. 6, the most intense band arises from the $^5D_0 \rightarrow {}^7F_2$ transition, which

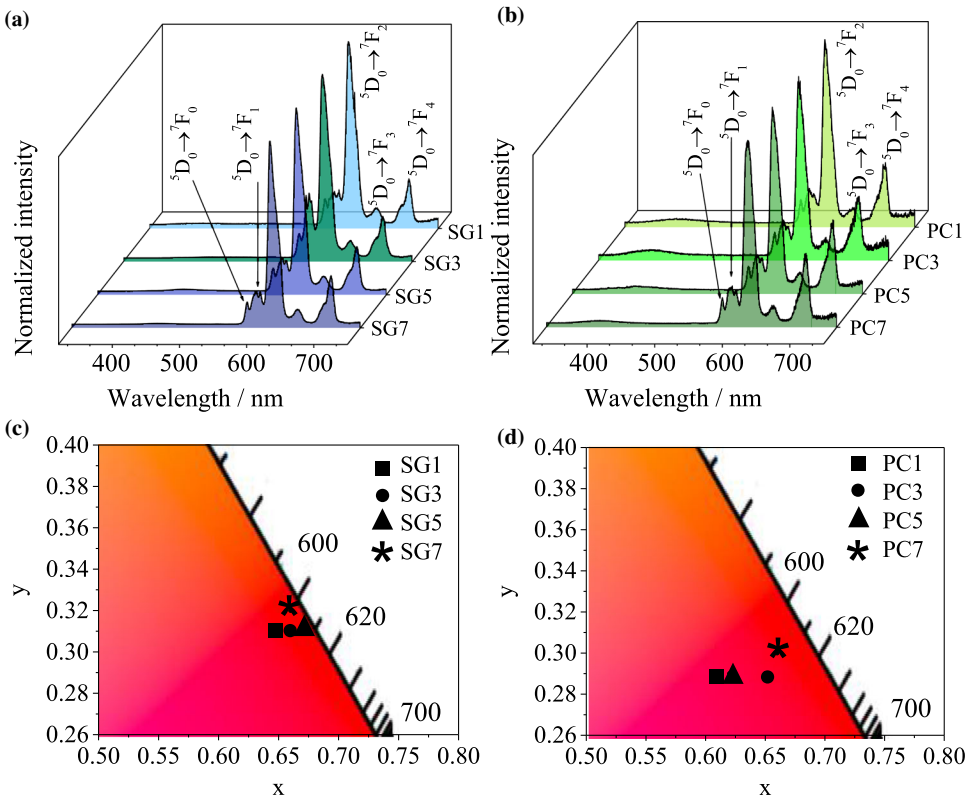

Figure 6 Emission spectra of **a** sol–gel and **b** Pechini-derived phosphors excited at 250 nm. 1,931 CIE chromaticity diagram of **c** sol–gel and **d** Pechini-derived phosphors.

occurs by a forced electric dipole mechanism, suggesting that Eu^{3+} is inserted in a low-symmetric site, in accordance with Eu^{3+} replacing Ba^{2+} local sites (C_1 or C_3 point group) within the $BaAl_2O_4$ lattice.

Eu^{3+} also enables a deep evaluation of the number of non-equivalent Eu^{3+} local sites with C_{nv}, C_n, and C_s point group since the $^5D_0$ state is non-degenerated, leading to only one component for the $^5D_0 \rightarrow {}^7F_0$ band for each non-equivalent Eu^{3+} local site according to the J rule ($2J + 1$) [49]. To get further insight on the Eu^{3+} local microssimmetry, low-temperature (77 K) selective excitation spectra were carried out in the range of the $^5D_0 \rightarrow {}^7F_0$ band for representative SG1, SG5, PC1, and PC5 phosphors, Fig. 7. PC1 and PC5 feature 1 and 2 $^5D_0 \rightarrow {}^7F_0$ transition components, respectively, suggesting that Eu^{3+} is inserted in at least two non-equivalent Eu^{3+} local sites, in accordance with Eu^{3+} replacing both Ba^{2+} sites in the $BaAl_2O_4$ lattice. On the other hand, SG1 and SG5 display 2 and 3 $^5D_0 \rightarrow {}^7F_0$ transition components, respectively, confirming that Eu^{3+} is inserted into 2 and 3 sites lacking inversion center. In this case, it must be highlighted that Eu^{3+} may replace Ba^{2+} into the $BaCO_3$ spurious phase found in low amounts in the sol–gel-derived samples.

Based on the Judd–Ofelt theory that describes the *f*-*f* emission of Ln^{3+} by the forced electric dipole mechanism, it is possible to determine Ω_2 and Ω_4 intensity parameters, Table 3. A study carried out by Malta and coworkers [50] has shown that the Ω_2 parameter is more influenced by angular distortions of the Eu^{3+}-ligand bond, in other words, its local microssymmetry, while Ω_4 suffers stronger influence of the Eu^{3+}-ligand bond polarizability.

The quite low Ω_4 values for samples reveal a predominant ionic nature of the Eu^{3+}–O^{2-} bonds, as expected since the Ba^{2+}-O^{2-} bonds are mainly ionic. For the Pechini-derived samples, the Ω_4 parameter increases from PC1 to PC3 and then, it decreases, suggesting an increase in the bond covalent degree up to the doping concentration of 3%. On the other hand, for the samples prepared by the sol–gel route, except for the SG3, the values are practically invariant; in these samples, it must be highlighted that the $BaCO_3$ spurious phase plays an important role in the

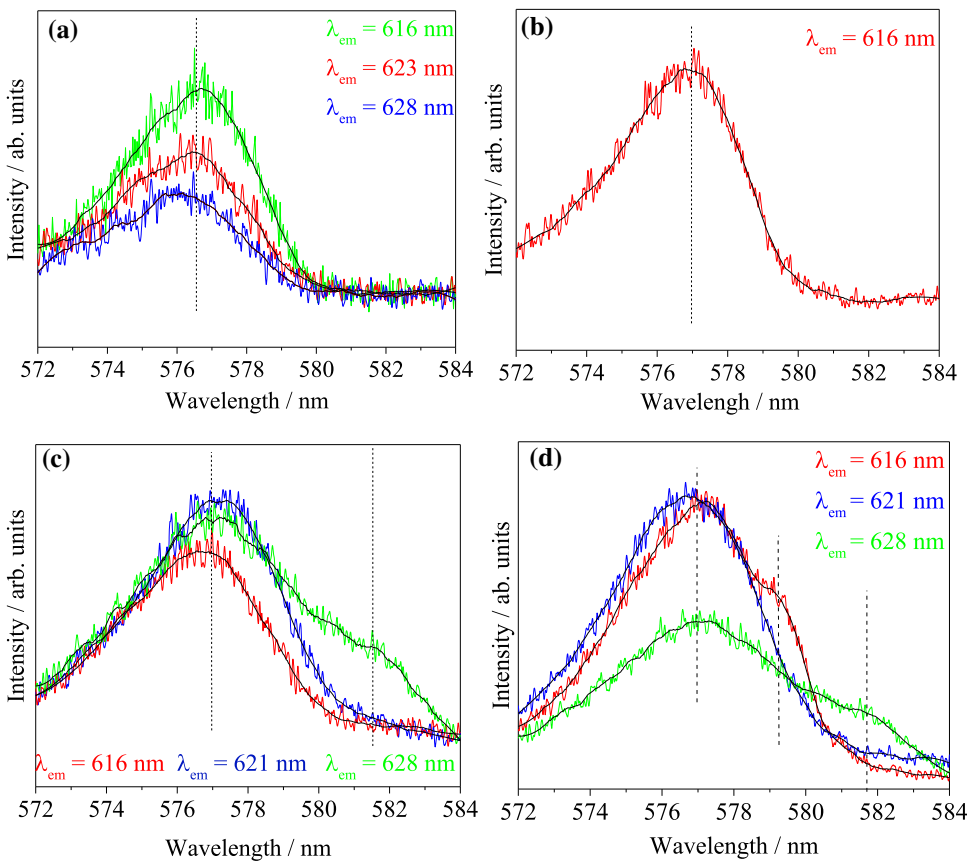

Figure 7 Selective excitation spectra (77 K, changing the emission wavelength, λ_{em}) within the $^5D_0 \rightarrow {}^7F_0$ transition range, monitoring the components of the $^5D_0 \rightarrow {}^7F_2$ transition (λ_{em}) for the **a** PC1, **b** PC5, **c** SG1 and **d** SG5 samples.

Table 3 Judd–Ofelt Ω_2 (10^{-20} cm^{-2}) and Ω_4 (10^{-20} cm^{-2}) intensity parameters, $^5D_0$ lifetime (τ / ± 0.01 ms) and average lifetime ($< \tau >$ / ± 0.01 ms), $^5D_0$ state radiative (A_{rad} / s^{-1}) and non-radiative (A_{nrad} / s^{-1}) decay probabilities, and intrinsic emission quantum yield (ϕ_{Ln}^{Ln}). The Eu^{3+}-Eu^{3+} critical distance (R_c, Å) is also shown

Sample	Ω_2	Ω_4	τ_1	τ_2	$< \tau >$	A_{rad}	A_{nrad}	ϕ_{Ln}^{Ln}	R_c
SG1	9.3	4.6	0.26	1.19	1.13	588	296	66	14
SG3	6.4	2.1	0.16	1.19	1.15	436	432	50	10
SG5	9.8	5.1	0.16	1.25	1.19	631	209	75	8.7
SG7	9.3	5.1	0.18	1.22	1.17	590	264	69	7.8
PC1	9.3	6.9	0.14	1.35	1.31	651	233	73	14
PC3	9.3	8.3	0.24	1.43	1.30	665	104	86	10
PC5	9.3	7.2	0.14	1.23	1.19	639	201	76	8.7
PC7	9.0	6.9	0.12	1.25	1.19	630	210	75	7.8

crystal growth as discussed by XRD, influencing the organization of the $BaAl_2O_4$ lattice.

The Ω_2 values are close for all Pechini-derived samples, suggesting that the Eu^{3+} concentration does not lead to significant changes on the Eu^{3+} local microssimetry, in accordance with the XRD data. However, samples synthesized by sol–gel display significant changes in the Ω_2 parameter as the Eu^{3+} amount increases, especially the SG3 sample. Again, in this case, the spurious phase may influence the network organization during the synthesis. As observed by the XRD data, Figure S2(a), the relative intensity of the peak at 24° assigned to $BaCO_3$ is not the same for all samples, suggesting that the weight fraction in the mixture is different. In this context, for the SG3 sample, the $BaCO_3$ weight fraction should be quite distinct from the others, causing deviations of the typical crystalline structure, especially modifications of Eu – O bond angles whose behavior influences the Ω_2 value.

The $^5D_0$ state lifetime values, Table 3, were obtained through a biexponential adjustment of the emission-decay curves shown in Figure S4. In this case, two $^5D_0$ state lifetime values were found and they were used to calculate an average lifetime by applying Eq. 6, where τ is the $^5D_0$ state lifetimes and A is a pre-exponential value obtained from the biexponential adjustment. The main importance of the lifetime value is the balance between the non-radiative (A_{nrad}) and radiative (A_{rad}) decay probabilities from the $^5D_0$ emitting state ($1/\tau = A_{rad} + A_{nrad}$). Thus, apart from the $^5D_0$ state lifetime value and the A_{rad} determined from Eq. 3, the intrinsic emission quantum yield of Eu^{3+} is defined as $\phi_{Ln}^{Ln} = A_{rad}/(A_{rad} + A_{nrad})$.

$$\tau = \frac{\sum A_i \tau_i^2}{\sum A_i \tau_i} \quad (6)$$

For all doping concentrations, the Pechini-derived phosphors feature the highest ϕ_{Ln}^{Ln}, confirming that the Pechini synthesis is the best route to get phosphors with better luminescent features. In the Pechini-derived series, ϕ_{Ln}^{Ln} increases from 1 to 3% of doping and then, it decreases, while for the phosphors obtained by the sol–gel route, ϕ_{Ln}^{Ln} enhances from 1 to 5%, and then it decreases, suggesting that the optimal doping concentration is around 3–5%, which is in accordance with a previous study reported for $BaAl_2O_3$:Eu^{3+} by R. Chatterjee and coworkers [15], implying that a quenching mechanism by concentration takes place from that on. This mechanism occurs because as the Eu^{3+} doping concentration increases, there occurs a shortening of the Eu–Eu distance within the $BaAl_2O_4$ lattice, increasing the energy transfer between them. However, this energy transfer may find network defects into the lattice, favoring non-radiative processes, enhancing the non-radiative decay probabilities, and as a consequence, decreasing ϕ_{Ln}^{Ln}.

Usually, this energy transfer among Ln^{3+} ions occurs non-radiatively by exchange or multipolar mechanisms [4]. The exchange mechanism contribution gains importance as the Ln^{3+}-Ln^{3+} distance decreases below 5 Å, since this mechanism occurs by electron transfer and requires a wide orbital overlap. Thus, the critical Ln^{3+}-Ln^{3+} distance within the

matrix is estimated by means of Eq. 7, where n_A is equal to $(x.n)/V$, and V is the unit cell volume (V = 830 Å^3, from the JCPD-17–0306 card) [15], x is the dopant concentration and n is the Ba^{2+} mol number per unit cell (n = 6 from the JCPD-17–0306 card) [15]. As the concentration increases, the Eu^{3+}-Eu^{3+} distance becomes shorter, suggesting that the exchange mechanism becomes relevant at higher doping concentrations.

$$R_C = \left(\frac{3}{4\pi n_A}\right)^{1/3} \quad (7)$$

To evaluate if the multipolar mechanism contributes to the energy transfer, the theoretical model developed by Van Uitert [51] was applied which is showed in Eq. 8, where x is the Eu^{3+} concentration, I is the emission intensity (A_{rad} was considered in this case), and β is a constant. In Eq. 8, θ is equal to 6 for dipole–dipole (D–D) interactions, 8 for electric dipole–quadrupole interactions, and 10 for electric quadrupole–quadrupole (Q–Q) interactions. In this sense, in a graphic of $\log(I/x)$ versus $\log(x)$, the slope of the curve is equal to $-\theta/3$. For both Pechini and sol–gel-derived samples, θ is 3 (Figure S5, supplementary material), suggesting that the multipolar mechanism is not relevant for the Eu^{3+}-Eu^{3+} energy transfer. Thus, the exchange mechanism is dominant on the Eu^{3+}-Eu^{3+} energy transfer in the samples featuring high Eu^{3+} concentration.

$$\frac{I}{x} = \left[1 + \beta(x)^{\theta/3}\right]^{-1} \quad (8)$$

By using ϕ_{Ln}^{Ln} as a figure of merit, Table 4, the phosphor efficiency is comparable with other typical red-emitting phosphors featuring high intrinsic emission quantum yield. Moreover, the value reported by us is also larger than the only value reported for $BaAl_2O_4$:Eu^{3+} by R. J. Wiglusz and coworkers, [11] which confirm that the Pechini route and the charge compensation mechanism are desirable strategies toward enhancing the luminescent features.

Finally, from the structural point of view, both sol–gel and Pechini methods enable the formation of highly crystalline and nanostructured $BaAl_2O_4$:Eu^{3+} red-emitting phosphor, although the sol–gel process also leads to the formation of traces of the $BaCO_3$ spurious phase. Moreover, the Pechini route is better to optimize the phosphor synthesis, leading to the highest intrinsic emission quantum yield (86% for PC3) and high emission color purity, which qualifies it for application as a UV-to-red downshifting converter phosphor.

Table 4 Comparison of $BaAl_2O_4$:Eu^{3+} with other red-emitting phosphors by using the intrinsic emission quantum yield (ϕ_{Ln}^{Ln}) as a figure of merit

Phosphor	ϕ_{Ln}^{Ln}/ %	References
$NaY(WO_4)_2$:Eu^{3+}	90	[52]
YOF:Eu^{3+}	96	[53]
Y_2O_3:Eu^{3+}	95	[54]
Ba_2SiO_4:Eu^{3+}	72	[25]
$Y_2(MoO_4)_3$:Eu^{3+}	92	[55]
$BaAl_2O_4$:Eu^{3+}	76	[11]
$BaAl_2O_4$:Eu^{3+}	86	This work

Conclusions

Herein, UV-to-red downshifting converter phosphors based on $BaAl_2O_4$:Eu^{3+} were synthesized by modified sol–gel or Pechini methods, performing a detailed investigation of luminescence, particle shape and structure. Both methods lead to highly crystalline samples and Eu^{3+} replaces Ba^{2+} within the $BaAl_2O_4$ lattice; yet, the sol–gel-derived samples display traces of $BaCO_3$ spurious phase. Moreover, under UV excitation, all phosphors feature emission with high color purity within the red spectral region as a result of electronic transitions from the Eu^{3+} $^5D_0$ state to the $^7F_{0\text{-}4}$ ones. Finally, the Pechini-derived sample doped with 3% of Eu^{3+} displays the largest intrinsic emission quantum yield (86%) reported so far for $BaAl_2O_4$:Eu^{3+}, qualifying it for application as a red-emitting phosphor.

Acknowledgements

Authors are thankful to the Brazilian agencies CNPq (Grant No. 304003/2018-2) and FAPESP for the financial research support. Laboratório de Microscopia Eletrônica de Varredura (FCT-UNESP, Prof. Dr. N. Alves), Laboratório de Materiais Cerâmicos (LaMaC, FCT-UNESP), and Laboratório Multiusuário de Análises Químicas (IQ/UNESP – Araraquara).

Declarations

Conflict of interest The authors declare that they have no conflict of interest.

Supplementary Information: The online version contains supplementary material available at https://doi.org/10.1007/s10853-021-06633-3.

References

[1] Moscardini SB, Sverzut L, Massarotto WL, Nassar EJ, Rocha LA (2020) Multi-color emission from lanthanide ions doped into niobium oxide. J Mater Sci Mater Electron 31:5241–5252. https://doi.org/10.1007/s10854-020-03084-5

[2] Kim CH, Kwon IE, Park CH, Hwang YJ, Bae HS, Yu BY, Pyun CH, Hong GY (2000) Phosphors for plasma display panels. J Alloys Compd 311:33–39. https://doi.org/10.1016/S0925-8388(00)00856-2

[3] Edgar A (2004–2021) Luminescent Materials. In: Kasap S, Capper P (eds) Springer Handbook of Electronic and Photonic Materials. Springer, Cham., pp. 1–1.

[4] Bispo-Jr AG, Lima SAM, Pires AM (2018) Energy transfer between terbium and europium ions in barium orthosilicate phosphors obtained from sol-gel route. J Lumin 199:372–378. https://doi.org/10.1016/j.jlumin.2018.03.057

[5] Wang L, Xie RJ, Suehiro T, Takeda T, Hirosaki N (2018) Down-Conversion nitride materials for solid state lighting: recent advances and perspectives. Chem Rev 118:1951–2009. https://doi.org/10.1021/acs.chemrev.7b00284

[6] Bispo-Jr AG, Lima SAM, Carlos LD, Ferreira RAS, Pires AM (2020) Red-emitting coatings for multifunctional UV/Red emitting LEDs applied in plant circadian rhythm control. ECS J Solid State Sci Technol 9:016008. https://doi.org/10.1149/2.0122001JSS

[7] Bispo-Jr AG, Saraiva LF, Lima SAM, Pires AM, Davolos MR (2021) Recent prospects on phosphor-converted LEDs for lighting, displays, phototherapy, and indoor farming. J Lumin 237:118167. https://doi.org/10.1016/j.jlumin.2021.118167

[8] Carlos LD, Ferreira RAS, Bermudez VZ, Julian-Lopez B, Escribano P (2011) Progress on lanthanide-based organic–inorganic hybrid phosphors. Chem Soc Rev 40:536–549. https://doi.org/10.1039/c0cs00069h

[9] Kaur J, Jaykumar B, Dubey V, Shrivastava R, Suryanarayana NS (2015) Optical properties of rare earth-doped barium aluminate synthesized by different methods-A Review. Res Chem Intermed 41:2317–2343. https://doi.org/10.1007/s11164-013-1349-z

[10] Shimokawa Y, Sakaida S, Iwata S, Inoue K, Honda S, Iwamoto Y (2015) Synthesis and characterization of Eu^{3+} doped $CaZrO_3$-based perovskite type phosphors part II: PL properties related to the two different dominant Eu^{3+} substitution sites. J Lumin 157:113–118. https://doi.org/10.1016/j.jlumin.2014.08.042

[11] Wiglusz RJ, Grzyb T (2013) Sol–gel synthesis of micro and nanocrystalline $BaAl_2O_4:Eu^{3+}$ powders and their luminescence properties. Opt Mater 36:539–545. https://doi.org/10.1016/j.optmat.2013.10.029

[12] Binnemans K (2015) Interpretation of europium(III) spectra. Coord Chem Rev 295:1–45. https://doi.org/10.1016/j.ccr.2015.02.015

[13] Nakauchi D, Okada G, Kato T, Kawaguchi N, Yanagida T (2020) Crystal growth and scintillation properties of $Eu:BaAl_2O_4$ crystals. Radiat Meas 135:106365. https://doi.org/10.1016/j.radmeas.2020.106365

[14] Raia RK, Upadhyay AK, Kher RS, Dhoble SJ, Mehta M (2011) $BaAl_2O_4$: Eu - Phosphor for mechanoluminescence dosimetry. Radiat Meas 46:1393–1396. https://doi.org/10.1016/j.radmeas.2011.08.016

[15] Chatterjee R, Saha S, Sen D, Panigrahi K, Ghorai UK, Das GC, Chattopadhyay KK (2018) Neutralizing the Charge Imbalance Problem in Eu^{3+}-Activated $BaAl_2O_4$ Nanophosphors: Theoretical Insights and Experimental Validation Considering K^+ Codoping. ACS Omega 3:788–800. https://doi.org/10.1021/acsomega.7b01525

[16] Marí B, Singh KC, Verma N, Mollar M, Jindal J (2015) Luminescence Properties of the Eu^{2+}/Eu^{3+} activated barium aluminate phosphors with Gd^{3+} concentration variation. Trans Ind Ceram Soc 74:1–5. https://doi.org/10.1080/0371750X.2015.1082932

[17] Grzeta B, Lutzenkirchen-Hecht D, Vrankic M, Bosnar S, Saric A, Takahashi M, Petrov D, Biscan M (2018) Environment of the Eu^{3+} ion within nanocrystalline Eu-Doped $BaAl_2O_4$: correlation of X-ray diffraction, mossbauer spectroscopy, X-ray absorption spectroscopy, and photoluminescence investigations. Inorg Chem 57:1744–1756. https://doi.org/10.1021/acs.inorgchem.7b02322

[18] Rezende MVS, Montes PJR, Andrade AB, Macedo ZS, Valerio MEG (2016) Mechanism of X-ray excited optical luminescence (XEOL) in europium doped $BaAl_2O_4$ phosphor. Phys Chem Chem Phys 18:17646. https://doi.org/10.1039/C6CP01183G

[19] Rezende MVS, Montes PJ, Valerio MEG, Jackson RA (2012) The optical properties of Eu^{3+} doped $BaAl_2O_4$: a computational and spectroscopic study. Opt Mater 34:1434–1439. https://doi.org/10.1016/j.optmat.2012.02.050

[20] Rezende MVS, Andrade AB, William C, Paschoal A (2018) Co-doping effect of Ca^{2+} on luminescent properties of $BaAl_2O_4:Eu^{3+}$ phosphors. J Electron Spectros Relat Phenomena 225:62–65. https://doi.org/10.1016/j.elspec.2018.04.002

[21] Araujo RM, Mattos EFS, Júnior BFS, Rezende MVS, Valerio MEG, Jackson RA (2021) Optical spectroscopy study of Eu-doped ions in $BaAl_2O_4$ phosphors. J Lumin 236:118011. https://doi.org/10.1016/j.jlumin.2021.118011

[22] Gomes MA, Andrade AB, Rezende MVS, Valerio MEG (2017) Production of Eu-doped $BaAl_2O_4$ at low temperature via an alternative solgel method using PVA as complexing agent. J Phys Chem Solids 102:74–78. https://doi.org/10.1016/j.jpcs.2016.11.010

[23] Verma N, Marí B, Singh KC, Jindal J, Yadav S, Mittal A (2019) Enhanced luminescence by tunable coupling of Eu^{3+} and Tb^{3+} in $ZnAl_2O_4:Eu^{3+}:Tb^{3+}$ phosphor synthesized by solution combustion method. J Aust Ceram Soc 55:179–185. https://doi.org/10.1007/s41779-018-0223-2

[24] Kumar N, Marí B, Jindal J, Mittal KK, Maken S (2019) Near ultraviolet excited down conversion Eu and Er co-doped $CaAl_2O_4$ color tunable nano-phosphors: Structural, morphological and photolumniscent characteristics. Mater Today Proc 19:646–649. https://doi.org/10.1016/j.matpr.2019.07.747

[25] Bispo-Jr AG, Ceccato DA, Lima SAM, Pires AM (2017) Red phosphor based on Eu^{3+}-isoelectronically doped Ba_2SiO_4 obtained via sol–gel route for solid state lightning. RSC Adv 7:53752. https://doi.org/10.1039/C7RA10494D

[26] Oliveira NA, Bispo-Jr AG, Shinohara GMM, Lima SAM, Pires AM (2021) The influence of the complexing agent on the luminescence of multicolor-emitting $Y_2O_3:Eu^{3+}$, $E^{r3}+$, $^{Yb}3+$ phosphors obtained by the Pechini's method. Mater Chem Phys 257:123840. https://doi.org/10.1016/j.matchemphys.2020.123840

[27] Aflaki M, Davar F (2016) Synthesis, luminescence and photocatalyst properties of zirconita nanosheets by modified Pechini method. J Mol Liq 221:1071–1079. https://doi.org/10.1016/j.molliq.2016.06.067

[28] Loghman-Estarki MR, Razavi RS, Edris H, Pourbafrany M, Jamali H, Ghasemi R, Lifetime of new SYSZ thermal barrier coatings produced by plasma spraying method under thermal shock test and high temperature treatment. Ceram Int 40:1405–1414. https://doi.org/10.1016/j.ceramint.2013.07.023

[29] Patterson AL (1939) The Scherrer formula for X-ray particle size determination. Phys Rev 56:978. https://doi.org/10.1103/PhysRev.56.978

[30] Murphy AB (2007) Band-gap determination from diffuse reflectance measurements of semiconductor films, and application to photoelectrochemicalwater-splitting. Sol Energy Mater Sol Cells 91:1326–1337. https://doi.org/10.1016/j.solmat.2007.05.005

[31] Kubelka P, Munk F (1931) EinBeitragzurOptik der Farbanstriche. Z Tech Phys 15:593–601

[32] Duarte AP, Gressier M, Menu M, Dexpert-Ghys J, Caiut JMA, Ribeiro SJL (2012) Structural and luminescence properties of silica-based hybrids containing new Silylated-Diketonato Europium(III) Complex. J Phys Chem C 116:505–515. https://doi.org/10.1021/jp210338t

[33] Weber MJ, (2002) Handbook of Optical Materials, first ed., CRC Press.

[34] Kodaira C, Brito HF, Malta OL, Serra OA (2003) Luminescence and energy transfer of the europium (III) tungstate obtained via the Pechini method. J Lumin 101:11–21. https://doi.org/10.1016/S0022-2313(02)00384-8

[35] Bispo-Jr AG, Lima SAM, Lanfredi S, Praxedes FR, Pires AM (2019) Tunable blue-green emission and energy transfer properties in $Ba_2SiO_4:Tb^{3+}$ obtained from sol-gel method. J Lumin 214:116604. https://doi.org/10.1016/j.jlumin.2019.116604

[36] Phule PP, Risbud SH (1980) Low-temperature synthesis and processing of electronic materials in the BaO-TiO_2 system. J Mater Sci 25:1169–2118. https://doi.org/10.1007/BF00585422

[37] López MDCB, Fourlaris G, Rand B, Riley FL (1999) Characterization of barium titanate powders: Barium carbonate identification. J Am Ceram Soc 82:1777–1786. https://doi.org/10.1111/j.1151-2916.1999.tb01999.x

[38] Andrade-Espinosa G, Escobar-Barrios V, Rangel-Mendez R (2010) Synthesis and characterization of silica xerogels obtained via fast sol–gel process. Colloid Polym Sci 288:1697–1704. https://doi.org/10.1007/s00396-010-2311-x

[39] Brinker CJ, Scherrer GW (1990) Sol-gel science, the physics and chemistry of sol-gel processing. Academic, San Diego

[40] Perullini M, Jobbagy M, Bilmes SA, Torriani IL, Candal R (2011) Effect of synthesis conditions on the microstructure of TEOS derived silica hydrogels synthesized by the alcohol-free sol–gel route. J Sol-Gel Sci Technol 59:174–180. https://doi.org/10.1007/s10971-011-2478-8

[41] Amaral FA, Santana LK, Campos IO, Fagundes WS, Xavier FFS, Canobre SC, Pechini Synthesis of Nanostructured $Li_{1.05}M_{0.02}Mn_{1.98}O_4$ (M = Al^{3+} or Ga^{3+}). Mater Res 18:250–259. doi: https://doi.org/10.1590/1516-1439.361514

[42] Loghman-Estarki MR, Hajizadeh-Oghaz M, Edris H, RS, (2013) Comparative studies on synthesis of nanocrystalline Sc_2O_3–Y_2O_3 doped zirconia (SYDZ) and YSZ solid solution via modified and classic Pechini method. Cryst Eng Comm 15:5898–5909. https://doi.org/10.1039/C3CE40288F

[43] Macedo WC, Bispo-Jr AG, Rocha KO, Albas AES, Pires AM, Teixeira SR, Longo E (2020) Photoluminescence of Eu^{3+}-doped $CaZrO_3$ red-emitting phosphors synthesized via microwave-assisted hydrothermal method. Mater Today Commun 24:100966. https://doi.org/10.1016/j.mtcomm.2020.100966

[44] Hiratsuka RS, Santili CV, Pulcinelli SH, (1995) O processo sol-gel:uma visão físico-química. Quim. Nova 18:171–180. https://doi.org/10.21577/0100-4042.20170623

[45] Oliveira HFN, Trinca RB, Gushikem Y (2009) Síntese e estudo de ortossilicatos de zinco luminescentes com aplicação da técnica sol-gel. Quim Nova 32:1346. https://doi.org/10.1590/S0100-40422009000500045

[46] Zhang LW, Wang L, Zhu YF, Synthesis and performance of $BaAl_2O_4$ with a wide spectral range of optical absorption. Adv Funct Mater 17:3781–3790. doi: https://doi.org/10.1002/adfm.200700506

[47] Carnall, WT, Crosswhite, H, Crosswhite, HM (1978) Energy level structure and transition probabilities in the spectra of the trivalent lanthanides in LaF_2. USDOE Office of Science, United States.

[48] Tanner PA (2013) Some misconceptions concerning the electronic spectra of tri-positive europium and cerium. Chem Soc Rev 42:5090–5101. https://doi.org/10.1039/C3CS60033E

[49] Tanner PA, Yeung YY, Ning L (2013) What Factors Affect the $^5D_0$ Energy of Eu^{3+}? An investigation of nephelauxetic effects. J Phys Chem A 117:2771–2781. https://doi.org/10.1021/jp400247r

[50] Moura RT, Neto ANC, Longo RL, Malta OL (2016) On the calculation and interpretation of covalency in the intensity parameters of 4f–4f transitions in Eu^{3+} complexes based on the chemical bond overlap polarizability. J Lumin 170:420. https://doi.org/10.1016/j.jlumin.2015.08.016

[51] Uitert LG (1967) Characterization of energy transfer interactions between rare earth ions. J Electrochem Soc 14:1048–1053. https://doi.org/10.1149/1.2424184

[52] Ting L, Qingyu M, Wenjun S (2015) Luminescent properties of Eu^{3+} doped $NaY(WO_4)_2$ nanophosphors prepared by molten salt method. J Rare Earths 33:915–921. https://doi.org/10.1016/S1002-0721(14)60505-6

[53] Grzyb T, Wecławiak M, Rozowska J, Lis S (2013) Structural and spectroscopic properties of YOF:Eu^{3+} nanocrystals. J Alloy Compd 576:345–349. https://doi.org/10.1016/j.jallcom.2013.05.207

[54] Som S, Das S, Dutta S, Visser HG, Pandey MK, Kumar P, Dubey RK, Sharma SK (2015) Synthesis of strong red emitting Y_2O_3:Eu^{3+} phosphor by potential chemical routes: comparative investigations on the structural evolutions, photometric properties and Judd-Ofelt analysis. RSC Adv 5:70887–70898. https://doi.org/10.1039/C5RA13247A

[55] Bispo-Jr AG, Shinohara GMM, Pires AM, Cardoso CX (2018) Red phosphor based on Eu^{3+}-doped $Y_2(MoO_4)_3$ incorporated with Au NPs synthesized via Pechini's method. Opt Mater 84:137–145. https://doi.org/10.1016/j.optmat.2018.06.023